ROYAL SOCIETY
OF CHEMISTRY

PAPER

Check for updates

Boosting anode kinetics in vanadium flow batteries with catalytic bismuth nanoparticle decorated carbon felt *via* electro-deoxidization processing†

Qi-an Zhang,[ab] Hui Yan,[a] Yuanfang Song,[a] Jing Yang,[a] Yuxi Song[a] and Ao Tang ✪ *[a]

Vanadium flow batteries (VFBs) have proven to be an ideal candidate for long-duration grid-scale energy storage. However, high power operation of VFBs is still impeded by the intrinsically sluggish kinetics of V^{2+}/V^{3+} redox reactions at the anode. Herein, we design catalytic bismuth nanoparticle dispersed carbon felt *via* facile one-step electro-deoxidization processing, which enables significantly enhanced anode redox kinetics for high-performance VFB operation. Experimental analyses together with theoretical calculations show that bismuth nanoparticles are successfully dispersed on carbon fibers *via* electro-deoxidization of bismuth oxide in alkaline solutions with an optimized loading content and applied voltage, which subsequently prove effective in catalyzing V^{2+}/V^{3+} redox reactions and thus significantly boost anode kinetics. First-principles calculation further unravels that the electrocatalytic effect of bismuth on V^{2+}/V^{3+} redox reactions is essentially attributable to both desirable vanadium adsorption/desorption and intensified d–p orbital hybridization between vanadium 3d and bismuth 6p orbitals that delicately modulate the surface electronic state and facilitate interfacial charge transfer. Consequently, the full VFB cell adopting bismuth nanoparticle decorated carbon felt at the anode acquires a significantly enhanced VE of 73.4% at 400 mA cm^{-2} and a highly stable EE of 73.6% at 350 mA cm^{-2} over 450 charge–discharge cycles.

Introduction

Reducing carbon dioxide emission is key to alleviating the rapidly changed global climate. Green energy technologies have seen a fast development over the past few decades so as to replace fossil fuels. Among them, solar and wind power are the glamorous twins of green energy revolution, and already produce approximately 10% of the world's electricity. By 2040, that share is expected to grow by five times, but concerns also arise as solar and wind cannot produce continual power reliably on their own. Thus, various energy storage technologies have been proposed to bridge the gap between clean energy generation and its reliability in grid use, and they typically include physical energy storage solutions (*e.g.*, pumped hydroelectric energy storage, compressed-air energy storage, *etc.*) and electrochemical energy storage systems such as rechargeable batteries. Compared with physical energy storage methods, rechargeable batteries have merits of high conversion efficiency and great flexibility in design and deployment, which have

become the most promising alternative to distributed energy systems.

Of all rechargeable battery technologies, the redox flow battery (RFB) adopting metal or organic redox actives dissolved in aqueous electrolyte solutions shows the greatest promise for grid applications,[1–3] as safety concerns in relation to fire and explosion of the battery are fully overcome. To date, various redox chemistries have been reported for use in redox flow batteries, such as iron–chromium RFBs,[4,5] all-vanadium RFBs,[6–8] zinc based RFBs,[9–11] all-iron RFBs,[12,13] organic RFBs,[14] *etc.*[15] Of all these RFBs, the all-vanadium flow batteries (VFBs) with the advantages of elimination of cross-contamination, high safety and flexibility in power and energy design have become the most attractive candidate for long-duration grid-scale energy storage applications. Despite successful deployments, highly efficient VFB operation is still, to some extent, hindered by the inferior redox chemistry of the V^{2+}/V^{3+} anode,[16–18] which can significantly compromise the charge–discharge efficiencies of the VFBs. The underlying reasons can be largely ascribed to the inherently sluggish kinetics of V^{2+}/V^{3+} redox reactions on commonly used porous carbon electrodes and meanwhile also partially attributable to the fact that the reduction potential of V^{3+} to V^{2+} and hydrogen evolution potential tend to be superimposed.

To tackle these issues, electrode modifications have attracted enormous attention, and tremendous effort has been made

[a]Institute of Metal Research, Chinese Academy of Sciences, Shenyang, China. E-mail: a. tang@imr.ac.cn

[b]College of Chemistry, Liaoning University, Shenyang, China

† Electronic supplementary information (ESI) available. See DOI: https://doi.org/10.1039/d2ta09909h

over the past decade to optimize carbon felt electrodes,[19–23] such as surface engineering,[17,24] heteroatom doping,[25,26] metal and metal oxide catalyst decoration,[27,28] *etc.*[29] While both surface engineering and heteroatom doping prove effective in enhancing anode V^{2+}/V^{3+} redox chemistry, only metal catalysts great promise to synergistically promote V^{2+}/V^{3+} kinetics and inhibit hydrogen evolution. For instance, bismuth presents a superior capability to catalyze V^{2+}/V^{3+} redox reactions,[30–32] while also bearing weak hydrogen adsorption free energy to deactivate the hydrogen evolution reaction proved by the volcano plot and computational high-throughput screening.[33] The existing methods to introduce a bismuth catalyst on carbon felt include one-step electrochemical deposition and multi-step thermal based reduction, such as electro-deposition in $FeCl_2$ solution and carbothermic reduction of Bi_2O_3.[32] Compared to relatively complicated multi-step approaches, the one-step modification method bears great benefits of fast processing and ease of use, which promise extraordinary potential for practical VFB applications. Hence, it is of vital importance to develop a new one-step method to effectively introduce bismuth catalysts on carbon felt electrodes for high-performance VFB operations.

Herein, we report a facile one-step electro-deoxidization processing strategy to decorate dispersed bismuth nanoparticles on carbon felt, which enables highly reversible V^{2+}/V^{3+} redox kinetics for high-performance VFB operations. Thermal dynamic calculations firstly reveal that bismuth oxide can be reduced *via* electro-deoxidization under alkaline conditions, while the subsequent optimization of the loading content and applied voltage in electro-deoxidization processing successfully yields bismuth nanoparticle dispersed carbon felt confirmed by morphology and composition analyses, which prove to effectively catalyze V^{2+}/V^{3+} redox reactions and significantly enhance the anode kinetics from electrochemical characterization. Theoretical calculations further uncover that the catalytic effect of bismuth on V^{2+}/V^{3+} redox chemistry essentially originates from both enhanced vanadium adsorption/desorption and strong d–p hybridization between vanadium and bismuth that effectively modulate the surface electronic state and facilitate electron transfer. With bismuth nanoparticle decorated carbon felt at the anode, the assembled vanadium flow cell demonstrates significantly promoted rate performance and long-term operation stability as compared to that using pristine CF, which offers substantial promise for advances in high-performance VFB design, fabrication and operation.

Experimental

Materials

Commercial carbon felt (3.8 mm thickness, Liaoning Jingu Carbon Material Co. Ltd.) was used as the raw material. Before the electro-deoxidization, freshly ground and dried Bi_2O_3 powder (20 wt%, 60 wt% and 100 wt% compared to the weight of carbon felt) was uniformly impregnated onto the carbon felt (geometric area 2 × 2 cm^2) by ultrasonic dispersion, which is denoted as the Bi_2O_3@CF precursor. Subsequently, the Bi_2O_3 powder coated on the carbon felt is electrochemically de-

oxidated to Bi metal (denoted as Bi@CF) in 50 wt% KOH solutions using a two-electrode system, in which the as-prepared precursor was placed at the cathode and platinum foil (2 × 2 cm^2) was used as the anode. To investigate the effect of applied potential for the electro-deoxidization processing, four different potentials (*i.e.*, 1.6 V, 1.8 V, 2.0 V, and 2.2 V) were applied to the two-electrode system. Prior to characterization, the as-prepared felt samples were washed with deionized water and dried in a vacuum oven at 120 °C.

Material characterization

The morphology of the carbon felt was characterized by using a scanning electron microscope (SEM, JEOL, JSM-6300, Japan) and transmission electron microscope (TEM, JEM 2100F), while the surface chemical states of the prepared samples were analyzed by X-ray photoelectron spectroscopy (XPS) (Thermo VG, EscaLab 250, USA) with Mg-Ka radiation (1253 eV, 250 W). Crystalline patterns were probed using X-ray diffraction (XRD) (PANalytical, X'pert PRO, Netherlands) with Cu Kα radiation, ranging from 10° to 90°. To gain more insights into the surface defects of the carbon felt, Raman spectroscopy (Renishaw, inVia, England) was performed from 1000 to 2000 cm^{-1} with 532 nm diode laser excitation. The hydrophilicity of the felt was evaluated by using a contact angle tester (Chengde Jinhe Technic Apparatus Co. Ltd., JC2000C1, China).

Electrochemical measurement

Cyclic voltammetry (CV), linear sweep voltammetry (LSV) and electrochemical impedance spectroscopy (EIS) tests were performed on an electrochemical workstation (Gamry, Reference 3000, USA) with a typical three-electrode system in a solution of 0.1 M $VOSO_4$ + 3 M H_2SO_4. The prepared felt was adopted as the working electrode, and a saturated calomel electrode (SCE) and platinum foil were applied as the reference electrode and counter electrode, respectively. The CV test was carried out with a voltage window ranging from −0.8 to −0.2 V *vs.* SCE for V^{2+}/V^{3+} redox reactions, while the voltage window for VO^{2+}/VO_2^+ ranged from 0 to 1.4 V *vs.* SCE at a scan rate of 10 mV s^{-1}. In addition, EIS tests were conducted at a fixed voltage of −0.5 V (*vs.* SCE) for V^{2+}/V^{3+} redox reactions in the frequency range from 100 kHz to 0.01 Hz with a perturbation of 5 mV. Based on the Randles–Sevcik equation, CV plots at varied scan rates were recorded to calculate vanadium diffusivity at the electrode–electrolyte interface. To assess the hydrogen evolution, LSV was conducted with a voltage window ranging from 0 to −1.2 V *vs.* SCE at a scan rate of 10 mV s^{-1}. EIS of the flow cell was also conducted to evaluate the fitted impedances, in which the electrolyte was charged to 50% SOC at a fixed flow rate of 80 mL min^{-1}.

Flow battery

An in-house designed flow battery was assembled, which is composed of aluminum alloy end plates, copper current collectors, graphite bipolar plates, a PVC flow frame, carbon felt electrodes and a perfluorinated sulfonic acid membrane (55 μm, Keking New Materials, China). The carbon felt with an

This journal is © The Royal Society of Chemistry 2023

J. Mater. Chem. A, 2023, **11**, 8700–8709 | **8701**

active geometric area of 2.0×2.0 cm^2 was compressed by *ca.* 20% in the flow cell assembly. 15 mL electrolyte of 1.0 M VO^{2+} in 3 M H$_2$SO$_4$ and 15 mL electrolyte of 1.0 M V^{3+} in 3 M H$_2$SO$_4$ were circularly pumped into the positive and negative sides respectively at a flow rate of 80 mL min^{-1}. The charge/discharge profiles of the flow cell were acquired in the voltage window of 0.9–1.65 V to avoid side reactions using a Neware battery tester (CT-4008T). Before the cycling tests, nitrogen gas was pumped into the electrolytes to expel air so as to avoid the potential side reactions.

Computational details

Density functional theory (DFT) calculations were carried out using the Quantum Espresso package. The generalized gradient approximation (GGA) with the Perdew–Burke–Ernzerhof (PBE) functional was employed for exchange-correlation energy. Geometry optimization was carried out by using the Broyden–Fletcher–Goldfarb–Shanno (BFGS) minimization with a tolerance on the maximal force of 0.001 Ha Bohr^{-1}, while the projector augmented wave (PAW) pseudopotentials were employed with a self-consistent field tolerance of 10^{-6} Ha. The kinetic energy cutoff and charge density cutoff were set to be 50 Ry and 641 Ry, respectively. The van der Waals (vdW) interactions were considered by using Grimme's DFT-D3 method. The slab models of Bi (012), Bi (104), Bi (110) and graphite (001) surfaces were constructed, and the k-point mesh in the Monkhorst-Pack scheme was set as $2 \times 2 \times 1$ for the Bi surface and $3 \times 3 \times 1$ for the graphite surface. To avoid the interaction caused by the periodicity, a vacuum layer of 20 Å along the z-direction was used for all calculations. The vanadium adsorption energy on the electrode surface E_{ads} was calculated by using $E_{ads} = E_{(V+surf)} - E_V - E_{surf}$, where $E_{(V+surf)}$ and E_{surf} are the total energies of the electrode surface with and without the vanadium atom adsorbed respectively, and E_V is the energy of an isolated vanadium atom. Crystal Occupation Hamilton Population (COHP) analysis was performed using LOBSTER software.

Results and discussion

Fig. 1a illustrates the processing of bismuth decorated carbon felt *via* the electro-deoxidization strategy, where bismuth oxides are coated onto the carbon felt and subsequently reduced to bismuth metal at the cathode in an electrolytic cell system. To select the optimal electro-deoxidization conditions, thermal dynamic calculations were firstly carried out. From Fig. 1b, it is seen that the thermodynamic redox potential of Bi$_2$O$_3$/Bi is 0.37 V, which is higher than that of hydrogen evolution (for details see the ESI†). Consequently, the reduction of Bi$_2$O$_3$ and oxygen evolution are expected to occur at the cathode and anode respectively during the electro-deoxidization process in the electrolytic cell with a theoretical open circuit voltage of 1.6 V. Fig. 1c further shows the potential variation as a function of the pH of solution, from which it indicates that increasing the pH can inhibit hydrogen evolution at the cathode and meanwhile reduce the cell voltage applied to the cell. Therefore, an alkaline solution of KOH is selected as the supporting electrolyte, which

can significantly enhance the efficiency of the electro-deoxidization process. To verify the theoretical calculation results, we further applied a voltage of 2 V to the electrolytic cell, where the cathode employs CF coated with Bi$_2$O$_3$. The current response shows a two-step process (*i.e.*, interfacial reaction and diffusion control) before it drops to zero (Fig. 1d), evidencing the complete reduction of Bi$_2$O$_3$ on CF at the cathode. The corresponding interfacial reaction mechanism of electro-deoxidization processing is schematically illustrated in Fig. 1e, where the coated Bi$_2$O$_3$ particles will be gradually reduced to bismuth on the surface of carbon fiber.

In order to verify the catalytic effect of bismuth on V^{2+}/V^{3+} redox chemistry and determine the appropriate loading of bismuth oxide for the electro-deoxidization, both electrochemical and morphology characterization were performed on pristine CF, as well as 20 wt%, 60 wt% and 100 wt% Bi$_2$O$_3$ loading CFs with electro-deoxidization processing at 2 V (Fig. 2a). CV results in Fig. 2b show that bismuth decorated CFs show a notable reduction peak of V^{3+} to V^{2+} at *ca.* −0.7 V with 20 wt% Bi$_2$O$_3$ loading presenting a remarkably enhanced redox reversibility, whereas pristine CF shows no clear reduction peak implying an inherently inferior anode redox chemistry. Aside from CVs, EIS results also indicate a much smaller charge transfer resistance for bismuth decorated CFs (Fig. 2c), confirming substantially promoted V^{2+}/V^{3+} redox kinetics. Moreover, both CV and EIS results suggest that a 20 wt% Bi$_2$O$_3$ loading outperforms the others in terms of catalyzing the anode redox reactions, as indicated in Fig. 2d by smaller separation of peak potentials (251 mV), the desirable ratio of peak currents ($i_{pc}/i_{pa} = 1$) and smaller charge transfer resistance ($R_{ct} = 91$ mΩ). By further comparing the SEM images, it is observed that 20 wt% Bi$_2$O$_3$ loading yields loose and small Bi particles on carbon fibers (Fig. 2e), which acts as an effective catalyst on CF to facilitate the kinetics of V^{2+}/V^{3+} as compared to pristine CF. When it comes to an excess Bi$_2$O$_3$ loading (*e.g.*, 100 wt%), by contrast, a dense coating can be observed on carbon fibers (Fig. S1†). Such a thick layer is possibly a mixture of Bi/Bi$_2$O$_3$, as the inside of the coating layer may contain incompletely reduced Bi$_2$O$_3$ particles owing to a greatly restricted diffusion of water molecules to trigger the electro-deoxidization (as illustrated in Fig. 1e). As a result, it may, to some extent, impede electron transfer and compromise the kinetics of V^{2+}/V^{3+} in comparison with a low Bi$_2$O$_3$ loading of 20 wt%, which is consistent with CV and EIS results observed above (Fig. 2b and c). Both electrochemical and morphology characterization prove that a low Bi$_2$O$_3$ loading of 20 wt% is preferred for the electro-deoxidization process at 2 V, but whether the applied voltage also affects the electro-deoxidization of Bi$_2$O$_3$ needs to be further elucidated.

In a bid to optimize the applied voltage, a voltage profile of the electro-deoxidization of Bi$_2$O$_3$ in the electrolytic cell at 10 mA cm^{-2} is given in Fig. 3a. As observed, the voltage starts from *ca.* 1.6 V and undergoes a plateau before it dramatically increases up to 2.4 V at which hydrogen evolution is triggered at the cathode (inset of Fig. 3a). Based on the voltage profile and to avoid hydrogen evolution, four different voltages ranging from 1.6 V to 2.2 V are then selected for a constant voltage based electro-deoxidization, and both the morphology and
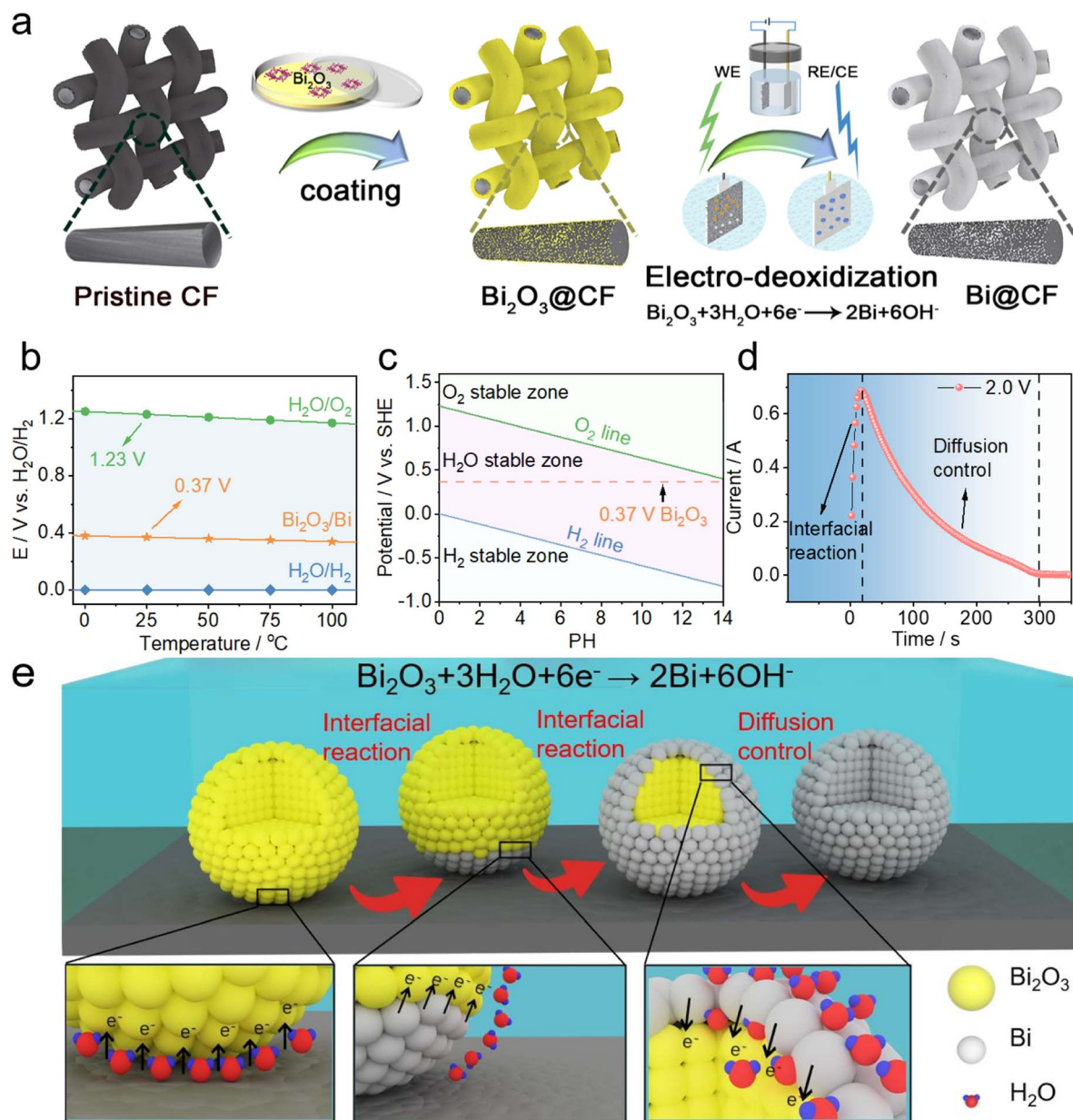
8702 | *J. Mater. Chem. A*, 2023, **11**, 8700–8709

This journal is © The Royal Society of Chemistry 2023

Fig. 1 (a) Schematic illustration of electro-deoxidization processing; (b) calculated standard potential profiles of Bi_2O_3/Bi, H_2O/O_2 and H_2O/H_2 in water as a function of temperature; (c) Pourbaix diagram of 50 wt% KOH solution at 25 °C; (d) current response of electro-deoxidization of Bi_2O_3 at 2 V; (e) schematic illustration of the interfacial reaction mechanism of electro-deoxidization processing.

electrochemical properties of the felt are compared in Fig. 3b. It is observed that as the applied voltage increases, large solid particles tend to be formed on carbon fibers after electro-deoxidization processing. By contrast, the electro-deoxidization processing under a low voltage of 1.6 V is more favorable for generating uniformly dispersed nanoparticles on carbon fibers, which turn out to be bismuth from EDX analysis (inset of Fig. 3b, and S2†). The observed bismuth nanoparticles coincide with the TEM image in Fig. 3c, where coated bismuth oxide particles also present a nano-scale structure with particle size ranging from 10 nm to 400 nm (Fig. S3†). The nanoparticles formed at low voltage of electro-deoxidization can be ascribed to

the resultant small current (Fig. S4†), which is in proportion to the formed particle size and such a small current effectively fines the bismuth formation during the electro-deoxidization process.[34] To further confirm the composition of the nanoparticles on carbon fibers, XPS was firstly carried out (Fig. S5†). Fig. 3d displays dominant Bi 4f, 4p and 4d peaks in the wide-range scan, while Fig. 3e depicts two prominent peaks at 157.1 and 162.4 eV in the deconvoluted Bi 4f peak, both indicating the existence of metallic bismuth reduced from bismuth oxides *via* electro-deoxidization processing at 1.6 V. Moreover, XRD results in Fig. 3f imply characteristic peaks located at 27°, 38° and 39.6° corresponding to Bi (012), Bi (104) and Bi (110)
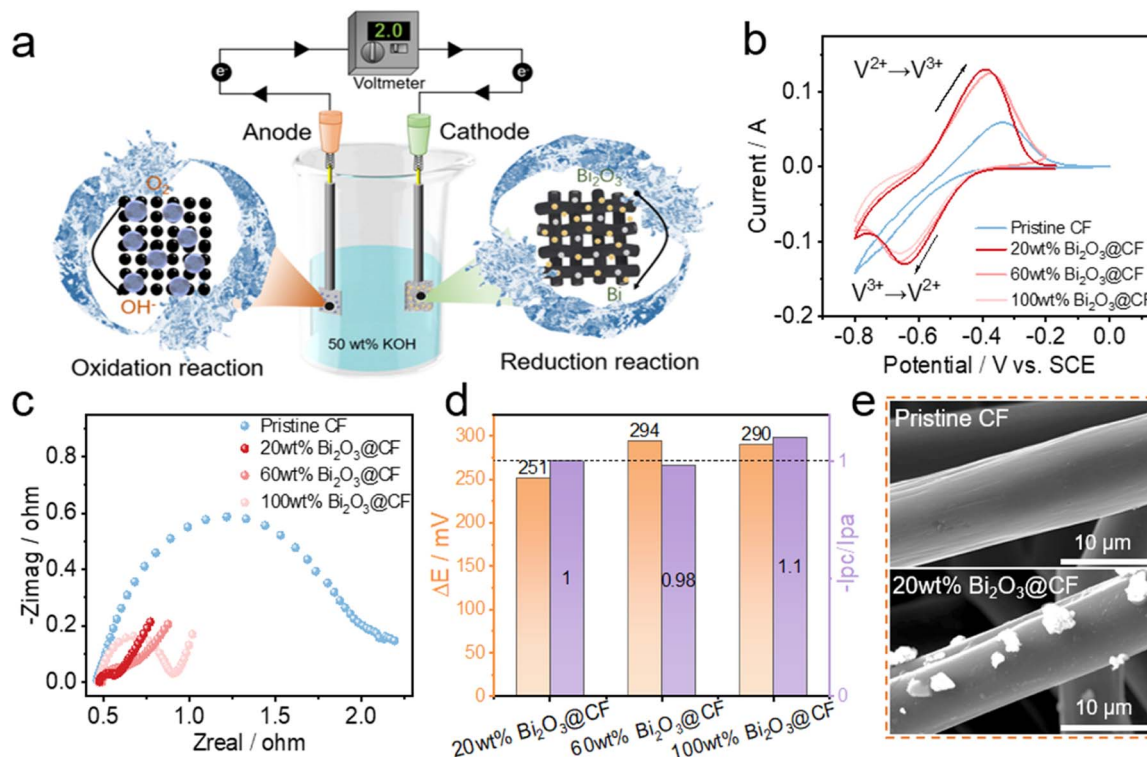
This journal is © The Royal Society of Chemistry 2023

J. Mater. Chem. A, 2023, 11, 8700–8709 | 8703

Fig. 2 (a) Schematic illustration of electro-deoxidization processing for Bi_2O_3 loaded CF at 2 V; (b) CV curves of the V^{2+}/V^{3+} redox reaction on CFs with varied Bi_2O_3 loadings; (c) Nyquist plots of the CFs with varied Bi_2O_3 loadings; (d) separation of peak potentials and the ratio of peak currents for different CF samples; (e) SEM morphologies of pristine CF and 20 wt% Bi_2O_3@CF after electro-deoxidization processing.

crystal planes respectively, further verifying the formation of bismuth on carbon felt.

After confirming successful decoration of bismuth on carbon felt *via* electro-deoxidization, electrochemical characterization is subsequently performed to evaluate the catalytic effect of bismuth on anode V^{2+}/V^{3+} reactions. CV results firstly compare the V^{2+}/V^{3+} reversibility on pristine CF and bismuth decorated CFs under various conditions (Fig. 3g). It can be seen from Fig. 3h that among the CF samples, the bismuth decorated CF at an electro-deoxidization processing voltage of 1.6 V shows both the smallest separation of peak potentials of 149 mV and a desirable ratio of peak currents (*i.e.*, $i_{pc}/i_{pa} = 1.01$), suggesting that dispersed bismuth nanoparticles effectively enhance the V^{2+}/V^{3+} reversibility. Besides, it is worth noting from the CV that for pristine CF, the reduction potential of V^{3+} is superimposed on that of hydrogen evolution (*i.e.*, the reduction of H^+ in Fig. S6†). In stark contrast, the bismuth nanoparticle decorated CF can yield a separated reduction peak of V^{3+} to V^{2+} at *ca.* −0.65 V and a lower hydrogen evolution potential of *ca.* −0.8 V, which manifests both significantly promoted V^{2+}/V^{3+} redox chemistry and effective suppression of hydrogen evolution. Moreover, EIS also shows the smallest charge transfer resistance for bismuth nanoparticle decorated CF at an electro-deoxidization potential of 1.6 V (Fig. 3i), further demonstrating the effectiveness of bismuth nanoparticles in catalyzing anode V^{2+}/V^{3+} kinetics on carbon felt. All the above analyses collectively validate that by electro-deoxidization processing of

bismuth oxide coated carbon felt at 1.6 V, catalytic bismuth nanoparticles can be readily formed on carbon fibers providing a low energy barrier for V^{2+}/V^{3+} redox reactions, which is responsible for the enhanced anode reversibility and electrode kinetics.

To further explore the electrochemical performance of bismuth nanoparticle dispersed CF, we subsequently perform the measurements of CV curves at varied scan rates. Fig. 4a and b show that as the scan rate rises the bismuth nanoparticle decorated CF still possesses a superior V^{2+}/V^{3+} reversibility in comparison to pristine CF, particularly with an increased reduction peak current alongside a complete cathodic peak. In contrast, the pristine CF shows no cathodic peak, implying an inferior reduction of V^{3+} to V^{2+} without bismuth catalyzing. Apart from that, plotting the peak current as a function of square root of scan rates based on the Randles–Sevcik equation yields a linear relationship suggesting a diffusion-controlled process (Fig. 4c), and the larger slopes of bismuth decorated CF reveal substantially enhanced mass transfer properties that significantly facilitate the anode kinetics consistent with the above EIS analyses. Additionally, Raman spectra further indicate a similar I_d/I_g ratio (Fig. 4d), signifying that electro-deoxidization processing has negligible impact on changing the surface of carbon fiber. This again verifies the fact that the enhancement in anode reversibility and kinetics essentially originates from the catalytic effect of bismuth nanoparticles. For bismuth decorated CF, furthermore, specific capacitance
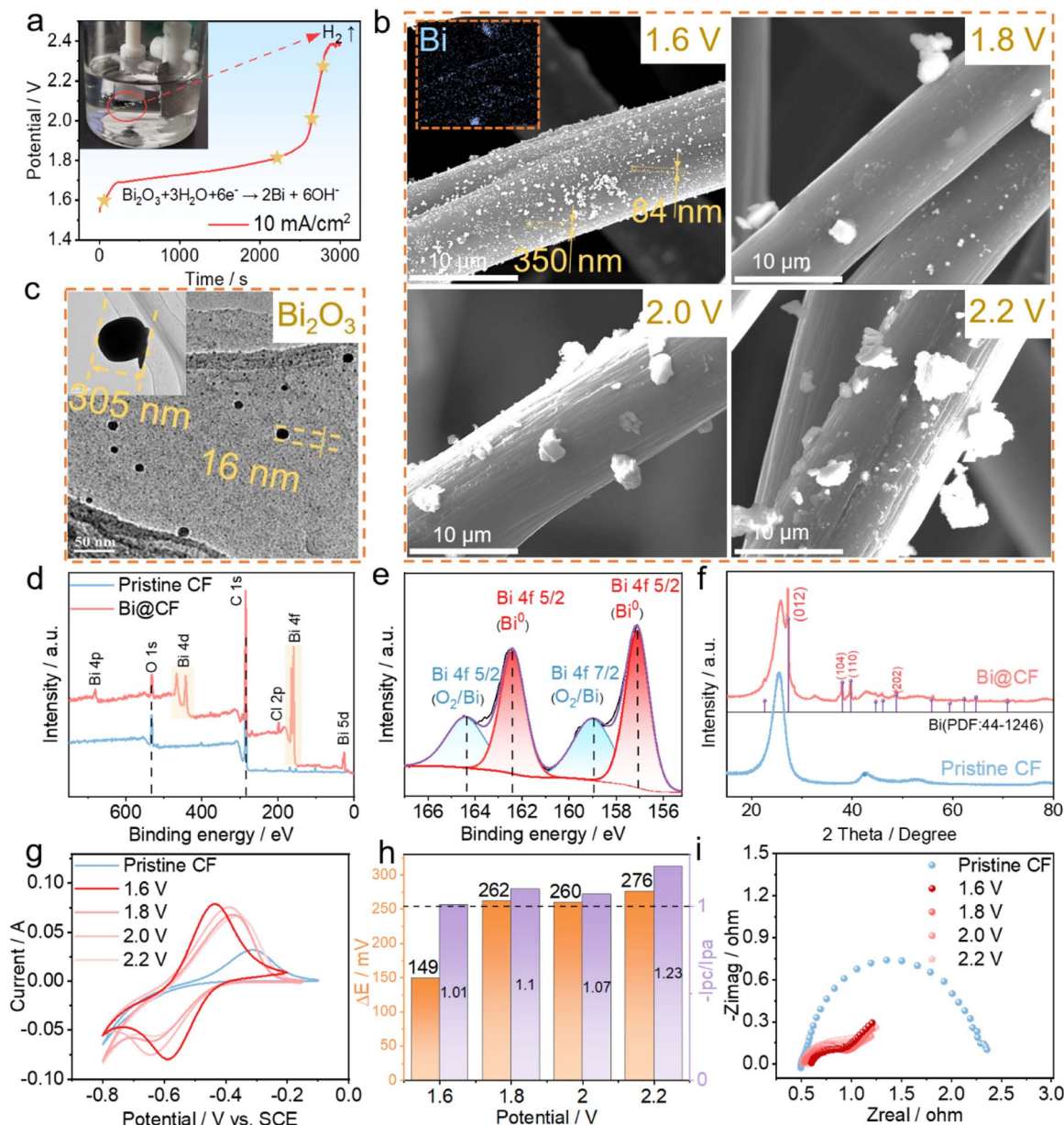
8704 | *J. Mater. Chem. A*, 2023, **11**, 8700–8709

This journal is © The Royal Society of Chemistry 2023

Fig. 3 (a) Voltage profile of electro-deoxidization processing at 10 mA cm^{-2}; (b) SEM morphologies of the CFs after electro-deoxidization processing at 1.6 V, 1.8 V, 2.0 V and 2.2 V; (c) TEM morphologies of Bi$_2$O$_3$ powder; (d) wide-scan XPS survey spectra; (e) the high-resolution Bi 4f spectra of pristine CF and Bi@CF; (f) XRD patterns of pristine CF and Bi@CF; (g) CV curves of V^{2+}/V^{3+} redox reactions on CFs with different electro-deoxidization processing potentials; (h) comparisons of separation of peak potentials and the ratio of peak currents; (i) Nyquist plots of different CF samples.

measurements clearly imply an approximate 4 times larger integrated area of the CV curve for bismuth decorated CF (Fig. 4e), which yields a value of 45 mF g^{-1} for bismuth decorated CF in comparison to 13 mF g^{-1} for pristine CF. Such a larger specific capacitance, together with an enhanced hydrophilicity observed from contact angle tests (Fig. 4f and S7†), again highlights the catalyzing effect of nanosized bismuth on boosting the anode V^{2+}/V^{3+} kinetics.

To understand the catalytic effect of bismuth nanoparticles on anode redox chemistry from atomic levels, first-principles calculations are performed. Fig. 4g firstly illustrates the

underlying mechanism of electrode kinetics for anode V^{2+}/V^{3+} reactions. As mass transfer is controlled by the flow rate in flow battery operation, the interfacial charge transfer process at the electrode surface is regarded as the rate-limiting step for the electrode kinetics of V^{2+}/V^{3+} reactions. According to XRD results in Fig. 3f, the adsorption of vanadium on three bismuth planes were calculated and the results in Fig. 4h indicate adsorption energy values of −4.87 eV, −3.33 eV and −6.06 eV for vanadium ions on Bi (012), Bi (104) and Bi (110) respectively, which are more negative than that of vanadium on graphite (−1.86 eV). The comparison suggests an enhanced adsorption capability for
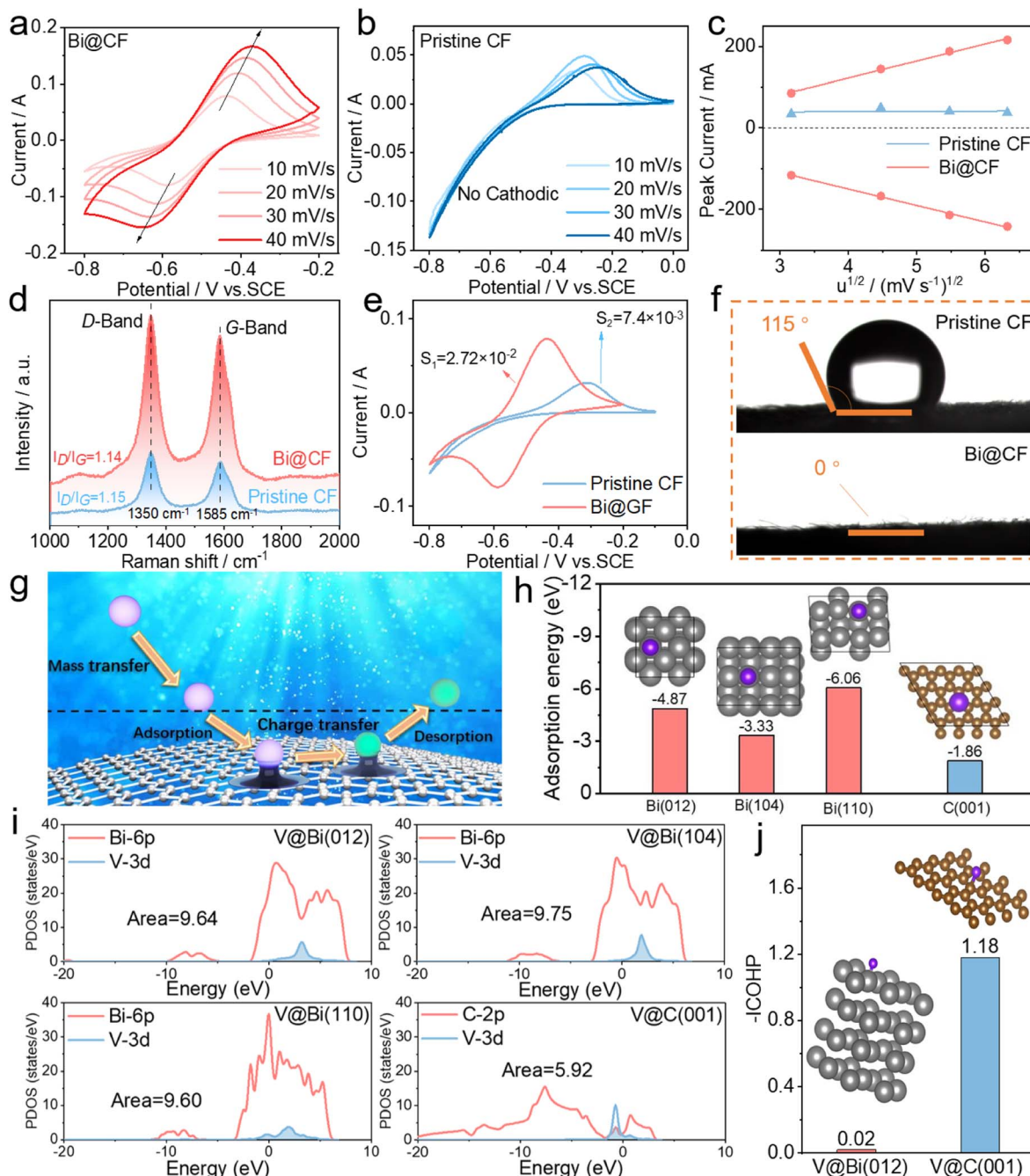
This journal is © The Royal Society of Chemistry 2023

J. Mater. Chem. A, 2023, 11, 8700–8709 | 8705

Fig. 4 CV curves of the V^{2+}/V^{3+} redox couple at varied scan rates: (a) Bi@CF and (b) pristine CF; (c) diffusivity for the V^{2+}/V^{3+} redox couple; (d) Raman spectra, (e) specific capacitance and (f) contact angle measurement of pristine CF and Bi@CF; (g) schematic diagram of electrode kinetics for V^{2+}/V^{3+} redox reactions on CF; (h) adsorption energy and (i) PDOS of vanadium on Bi (012), Bi (104), Bi (110) and C (001); (j) –ICOHP of vanadium on Bi (012) and C (001).

vanadium on bismuth, which is potentially beneficial for subsequent charge transfer between vanadium ions and the electrode. By further analyzing the partial density of states (PDOS), it is found in Fig. 4i that the graphite shows a small overlapped area of 5.92, corresponding to a weak d–p orbital hybridization between the vanadium 3d-orbital and graphite 2p-orbital. By contrast, the bismuth nanoparticles enable a significantly intensified d–p hybridization between vanadium

3d and bismuth 6p orbitals, as implied by a much larger over-lapped area over 9.6. Such an enhanced d–p orbital hybridiza-tion between vanadium and bismuth signifies an effective modulation of the electronic state of the electrode surface, which can significantly promote the charge transfer of anode V^{2+}/V^{3+} reactions. In addition to adsorption and charge transfer, the desorption process can also be related to the integrated COHP value that hints towards the bond strength. The V–Bi

8706 | *J. Mater. Chem. A*, 2023, **11**, 8700–8709

This journal is © The Royal Society of Chemistry 2023

bond strength between the vanadium ion and its adjacent Bi atom is evaluated by the integral of COHP between the Fermi level and minimum energy. Compared to C (001), Bi (012) with the strongest intensity in XRD yields a much smaller –ICOHP value (0.02 *vs.* 1.18), implying a weak V–Bi bond strength that can facilitate the desorption process and thus accelerate the interfacial electrode kinetics of V^{2+}/V^{3+} reactions. Therefore, it can be concluded that the catalytic effect of bismuth nanoparticles on anode redox chemistry is attributable to

a synergetic enhancement in vanadium adsorption/desorption and interfacial electron transfer.

In an attempt to fully assess the bismuth nanoparticle decorated CF, flow cell tests are finally carried out. As illustrated (Fig. 5a and b), adopting a bismuth nanoparticle decorated CF at the anode can allow a theoretical cell voltage of 1.4 V with enhanced anode reversibility and suppressed hydrogen evolution (Fig. S5†). Benefiting from bismuth catalyzing, Fig. 5c shows that at a high current density of 300 mA cm^{-2} the
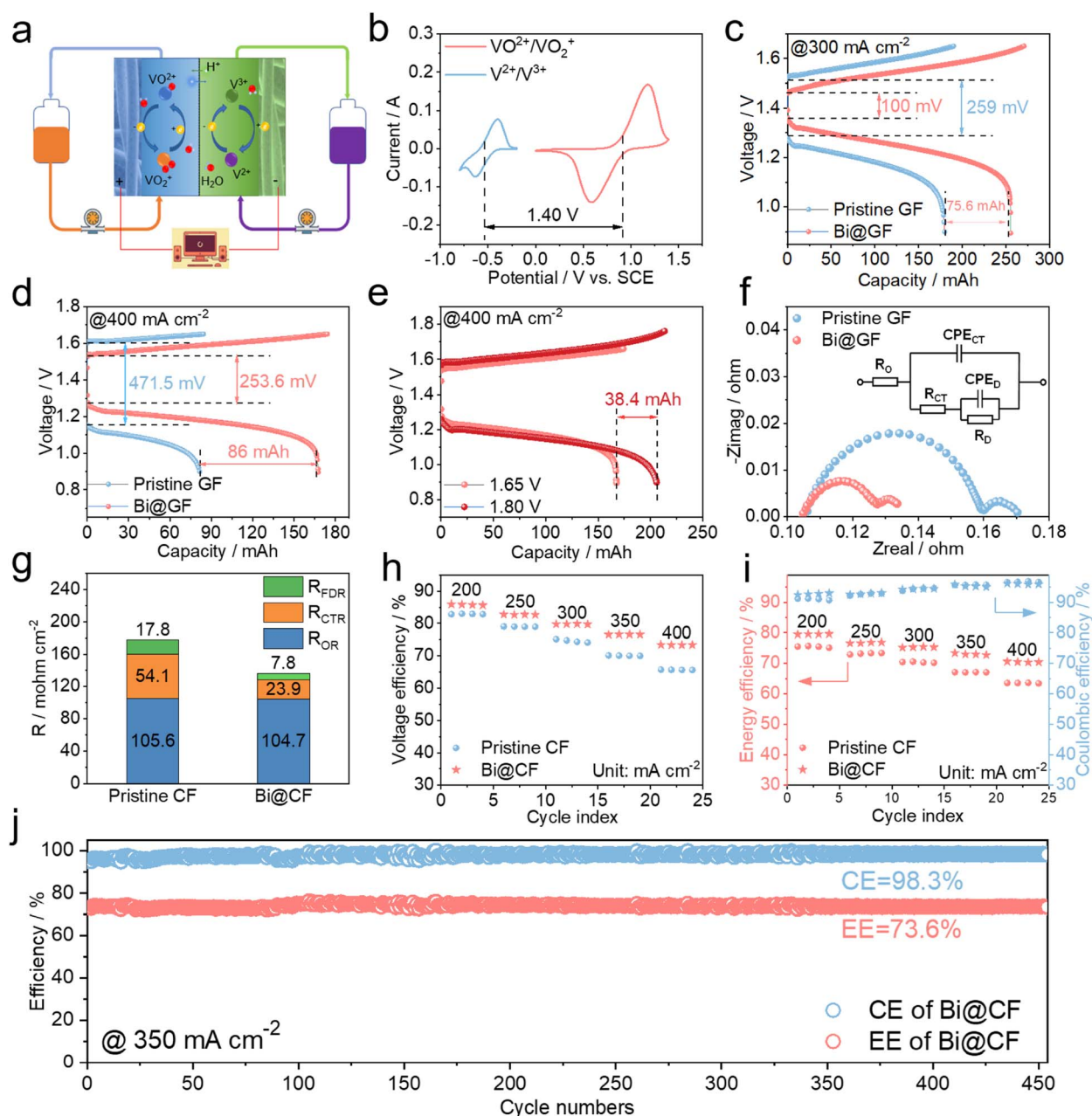

Fig. 5 (a) Schematic diagram of a VFB; (b) voltage window for the VFB adopting Bi@CF as the negative electrode; comparison of the charge–discharge curves of the VFBs at (c) 300 mA cm^{-2} and (d) 400 mA cm^{-2}; (e) charge–discharge curves of the VFB with Bi@CF at 400 mA cm^{-2} under different charging cut off limits; (f) Nyquist plots of the VFB using different CFs as negative electrodes; (g) fitted ohmic resistance (R_{OR}), charge transfer resistance (R_{CTR}) and diffusion resistance (R_{FDR}) with an equivalent circuit model; (h) VE, (i) CE and EE at different current densities; (j) long-term cycling performance of the VFB using Bi@CF as the negative electrode at 350 mA cm^{-2}.

This journal is © The Royal Society of Chemistry 2023

J. Mater. Chem. A, 2023, **11**, 8700–8709 | **8707**

vanadium flow cell using a bismuth decorated CF creates much smaller polarizations than that with pristine CF (*i.e.*, 100 mV *vs.* 259 mV), thereby providing a higher discharge capacity that substantially promotes the electrolyte utilization (*e.g.*, by 19%). When it comes to an increased current density of 400 mA cm^{-2}, the vanadium flow cell with bismuth decorated CF at the anode still outperforms the flow cell with pristine CF in terms of polarization and discharge capacity (Fig. 4d). By further lifting the charging voltage limit from 1.65 V to 1.8 V, the discharge capacity of the flow cell based on bismuth decorated CF is seen to be promoted by 38.4 mA h corresponding to *ca.* 10% increase in electrolyte utilization, suggesting that the as-fabricated bismuth decorated CF can enable a stable and high capacity delivery for VFB operation at very high operating current densities. To quantify the polarizations and probe the V^{2+}/V^{3+} kinetics, EIS was subsequently conducted on the flow cells with pristine CF and catalytic bismuth decorated CF at the anode. It is noted in Fig. 5f that both of the flow cells present a similar high-frequency resistance, while the flow cell with bismuth decorated CF at the anode has a high frequency semi-circle with greatly reduced radius, which corresponds to a smaller charge transfer resistance. Such a difference can be also revealed by fitting data into an electric circuit model (inset of Fig. 5f), where the charge transfer resistance of the flow cell is notably halved by adopting catalytic bismuth decorated CF at the anode (Fig. 5g). EIS analyses of the flow cells clearly prove that the surpassing performance of the flow cell with bismuth decorated CF in Fig. 5d– stems from the superior catalytic effect of bismuth nanoparticles on anode V^{2+}/V^{3+} kinetics. Furthermore, the rating performance of the vanadium flow cell is presented in Fig. 5h–i. Compared to pristine CF, the bismuth decorated CF is observed to yield remarkably enhanced VE and EE for the flow cell, *e.g.*, 73.4% VE and 70.6% EE at 400 mA cm^{-2}. Long-term operation of the vanadium flow cell finally shows that catalytic bismuth decorated CF can realize both a highly stable CE of 98.3% and EE of 73.6% at 350 mA cm^{-2} for 450 consecutive charge–discharge cycles, highlighting the effectiveness and superiority of catalytic bismuth nanoparticle decorated CF toward high-performance VFB operation through the proposed one-step electro-deoxidization processing strategy.

Conclusion

In summary, we design bismuth nanoparticle dispersed carbon felt *via* a facile one-step electro-deoxidization processing strategy, which enables highly reversible V^{2+}/V^{3+} redox kinetics for high-performance VFB operations. Thermal dynamic calculations firstly reveal that an alkaline solution can significantly enhance the efficiency of the electro-deoxidization process, which is subsequently confirmed in an electrolytic cell system with Bi_2O_3 completely reduced to bismuth on CF in KOH. Electrochemical and morphology characterization further verify the catalytic effect of bismuth on V^{2+}/V^{3+} redox chemistry and prove that a low Bi_2O_3 loading of 20 wt% can yield uniformly dispersed bismuth nanoparticles on CF at a low voltage of 1.6 V in the electro-deoxidization processing. Compared to pristine CF, the bismuth nanoparticle decorated

CF demonstrates significantly enhanced V^{2+}/V^{3+} redox reversibility and electrode kinetics as revealed by CV and EIS tests. DFT calculations at the atomic level further uncover that the bismuth not only facilitates interfacial vanadium adsorption/ desorption but also enables strong d–p hybridization between V-3d and Bi-6p orbitals, which synergistically boost the electrode kinetics of V^{2+}/V^{3+} reactions. Benefitting from substantially enhanced anode kinetics, the assembled VFB cell shows a dramatically reduced polarization and consequently acquires a remarkably enhanced VE of 73.4% and EE of 70.6% at 400 mA cm^{-2}. Besides, long-term operation of the VFB also demonstrates that catalytic bismuth decorated CF can realize both a highly stable CE of 98.3% and EE of 73.6% at 350 mA cm^{-2} for 450 consecutive charge–discharge cycles. This study not only offers an alternative to existing methods for fabricating metal catalysts (not limited to bismuth) on carbon felt electrodes *via* electro-deoxidization processing, but also sheds light on the underlying mechanism of metal catalysts towards remarkably enhanced V^{2+}/V^{3+} redox kinetics at the atomic level, which should be highly valued to guide future development of high-performance electrodes for vanadium flow batteries.

Author contributions

Qi-an Zhang: conceptualization, investigation, validation, visualization, and Writing–Original Draft. Hui Yan: investigation and software. Yuanfang Song: investigation and software. Jing Yang: investigation and software. Yuxi Song: investigation and validation. Ao Tang: investigation, writing – review & editing, resources, supervision, project administration, and funding acquisition.

Conflicts of interest

There are no conflicts to declare.

Acknowledgements

References

1 L. Tang, P. Leung, Q. Xu, M. Mohamed, S. Dai, X. Zhu, C. Flox and A. Shah, *Curr. Opin. Chem. Eng.*, 2022, **37**, 100833.
2 T. Xuan and L. Wang, *Energy Storage Mater.*, 2022, **48**, 263– 282.
3 R. Emmett and M. Roberts, *J. Power Sources*, 2021, **506**, 230087.
4 Y. Ahn, J. Moon, S. Park, J. Shin, J. Choi and K. Kim, *Chem. Eng. J.*, 2021, **421**, 127855.
5 B. Robb, J. Farrell and M. Marshak, *Joule*, 2019, **3**, 2503–2512.
6 J. Kim and H. Park, *J. Power Sources*, 2022, **545**, 231904.
7 A. Trovò, N. Poli and M. Guarnieri, *Curr. Opin. Chem. Eng.*, 2022, **37**, 100853.
8 H. Hao, Q. Zhang, Z. Feng and A. Tang, *Chem. Eng. J.*, 2022, **450**, 138170.

8708 | *J. Mater. Chem. A*, 2023, **11**, 8700–8709

This journal is © The Royal Society of Chemistry 2023

9 M. Mousavi, H. Dou, H. Fathiannasab, C. Silva, A. Yu and Z. Chen, *Chem. Eng. J.*, 2021, **412**, 128499.

10 J. Yang, H. Yan, H. Hao, Y. Song, Y. Li, Q. Liu and A. Tang, *ACS Energy Lett.*, 2022, **7**, 2331–2339.

11 Z. Yuan, Y. Yin, C. Xie, H. Zhang, Y. Yao and X. Li, *Adv. Mater.*, 2019, **31**, 1902025.

12 Y. Song, K. Zhang, X. Li, C. Yan, Q. Liu and A. Tang, *J. Mater. Chem. A*, 2021, **9**, 26354.

13 H. Zhang and C. Sun, *J. Power Sources*, 2021, **493**, 229445.

14 C. Zhang and X. Li, *Curr. Opin. Electrochem.*, 2021, **30**, 100836.

15 Z. Li and Y. C. Lu, *Nat. Energy*, 2021, **6**, 517–528.

16 K. Zhang, C. Yan and A. Tang, *Energy Storage Mater.*, 2021, **34**, 301–310.

17 R. Huang, S. Liu, Z. He, W. Zhu, G. Ye, Y. Su, W. Deng and J. Wang, *Adv. Funct. Mater.*, 2022, **32**, 2111661.

18 J. Qiu, B. Huang, Y. Liu, D. Chen and Z. Xie, *J. Energy Chem.*, 2020, **45**, 31–39.

19 K. Amini and J. Gostick, *Adv. Funct. Mater.*, 2020, **30**, 1910564.

20 Z. He, Y. Lv, T. Zhang, Y. Zhu, L. Dai, S. Yao, W. Zhu and L. Wang, *Chem. Eng. J.*, 2022, **437**, 131680.

21 Z. Hu, Z. Miao, Z. Xu, X. Zhu, F. Zhong, M. Ding, J. Wang, X. Xie, C. Jia and J. Liu, *Chem. Eng. J.*, 2022, **450**, 138377.

22 Y. Jiang, Z. Liu, Y. Lv, A. Tang, L. Dai, L. Wang and Z. He, *Chem. Eng. J.*, 2022, **443**, 136341.

23 Y. Jiang, G. Cheng, Y. Li, Z. He, J. Zhu, W. Meng, L. Dai and L. Wang, *Chem. Eng. J.*, 2021, **415**, 129014.

24 A. Mukhopadhyay, Y. Yang, Y. Li, Y. Chen, H. Li, A. Natan, Y. Liu, D. Cao and H. Zhu, *Adv. Funct. Mater.*, 2019, **29**, 1903192.

25 K. Zhang, C. Yan and A. Tang, *J. Mater. Chem. A*, 2021, **9**, 17300.

26 Y. Liu, L. Yu, X. Liu, L. Liu and J. Xi, *J. Energy Chem.*, 2022, **72**, 545–553.

27 H. R. Jiang, W. Shyy, L. Zeng, R. H. Zhang and T. S. Zhao, *J. Mater. Chem. A*, 2018, **6**, 13244.

28 X. Zhou, X. Zhang, Y. Lv, L. Lin and Q. Wu, *Carbon*, 2019, **153**, 674–681.

29 X. Zhang, D. Zhang, Z. Xu, K. Zhang, Y. Zhang, M. Jing, L. Liu, Z. Zhang, N. Pu, J. Liu and C. Yan, *Chem. Eng. J.*, 2021, **439**, 135718.

30 B. Li, M. Gu, Z. Nie, Y. Shao, Q. Luo, X. Wei, X. Li, J. Xiao, C. Wang, V. Sprenkle and W. Wang, *Nano Lett.*, 2013, **13**, 1330–1335.

31 X. Zhang, X. Ye, S. Huang and X. Zhou, *ACS Appl. Mater. Interfaces*, 2021, **13**, 37111–37122.

32 X. Zhou, X. Zhang, L. Mo, X. Zhou and Q. Wu, *Small*, 2020, **16**, 1907333.

33 J. Greeley, T. F. Jaramillo, J. Boned, I. Chorkendorff and J. K. Nørskov, *Nat. Mater.*, 2004, **3**, 810–815.

34 A. M. Rashidi and A. Amadeh, *Surf. Coat. Technol.*, 2008, **202**, 3772–3776.

This journal is © The Royal Society of Chemistry 2023

J. Mater. Chem. A, 2023, **11**, 8700–8709 | 8709